

Article

Excellent Catalytic Performance of ISOBAM Stabilized Co/Fe Colloidal Catalysts toward KBH_4 Hydrolysis

Keke Guan ^{1,†}, Qing Zhu ^{1,†}, Zhong Huang ^{1,*}, Zhenxia Huang ^{1,2}, Haijun Zhang ^{1,*}, Junkai Wang ^{1,2}, Quanli Jia ³ and Shaowei Zhang ⁴

¹ The State Key Laboratory of Refractories and Metallurgy, Wuhan University of Science and Technology, Wuhan 430081, China

² School of Materials Science and Engineering, Henan Polytechnic University, Jiaozuo 454003, China

³ Henan Key Laboratory of High Temperature Functional Ceramics, Zhengzhou University, Zhengzhou 450052, China

⁴ College of Engineering, Mathematics and Physical Sciences, University of Exeter, Exeter EX4 4QF, UK

* Correspondence: huangzhong@wust.edu.cn (Z.H.); zhanghaijun@wust.edu.cn (H.Z.)

† These authors contributed equally to this work.

Abstract: Recently, developing a cost-effective and high-performance catalyst is regarded as an urgent priority for hydrogen generation technology. In this work, ISOBAM-104 stabilized Co/Fe colloidal catalysts were prepared via a co-reduction method and used for the hydrogen generation from KBH_4 hydrolysis. The obtained ISOBAM-104 stabilized $\text{Co}_{10}\text{Fe}_{90}$ colloidal catalysts exhibit an outstanding catalytic activity of $37,900 \text{ mL-H}_2 \text{ min}^{-1} \text{ g-Co}^{-1}$, which is far higher than that of Fe or Co monometallic nanoparticles (MNPs). The apparent activation energy (E_a) of the as-prepared $\text{Co}_{10}\text{Fe}_{90}$ colloidal catalysts is only $14.6 \pm 0.7 \text{ kJ mol}^{-1}$, which is much lower than that of previous reported noble metal-based catalysts. The X-ray photoelectron spectroscopy results and density functional theory calculations demonstrate that the electron transfer between Fe and Co atoms is beneficial for the catalytic hydrolysis of KBH_4 .

Keywords: ISOBAM-104; Co/Fe colloidal catalysts; hydrogen generation; KBH_4 hydrolysis; catalytic activity



Citation: Guan, K.; Zhu, Q.; Huang, Z.; Huang, Z.; Zhang, H.; Wang, J.; Jia, Q.; Zhang, S. Excellent Catalytic Performance of ISOBAM Stabilized Co/Fe Colloidal Catalysts toward KBH_4 Hydrolysis. *Nanomaterials* **2022**, *12*, 2998. <https://doi.org/10.3390/nano12172998>

Academic Editors: Florian Ion Tiberiu Petrescu and Gang Shi

Received: 27 July 2022

Accepted: 26 August 2022

Published: 30 August 2022

Publisher's Note: MDPI stays neutral with regard to jurisdictional claims in published maps and institutional affiliations.



Copyright: © 2022 by the authors. Licensee MDPI, Basel, Switzerland. This article is an open access article distributed under the terms and conditions of the Creative Commons Attribution (CC BY) license (<https://creativecommons.org/licenses/by/4.0/>).

1. Introduction

Recently, hydrogen has been widely considered as a promising clean energy source to replace the traditional fossil fuels. Chemical hydrogen storage materials have aroused tremendous interest because of their inherent advantages such as high content of hydrogen, no toxicity, low hydrogen releasing temperature, and an easily controllable hydrogen generation process [1–8]. Among those materials, potassium borohydride (KBH_4) stands out owing to its safe production process, harmless hydrolysis product, low activation energy and enthalpy [9–14]. Unfortunately, the low hydrogen production rate of KBH_4 self-hydrolysis hinders its large-scale practical application.

Many researchers found that metal nanoparticles (NPs) could catalyze the hydrolysis of KBH_4 and accelerate the generation rate of hydrogen [7,15,16]. For example, Kilinc et al. [7] successfully prepared the Pd complex catalysts for promoting the KBH_4 hydrolysis. The catalytic activity of the as-prepared catalysts was up to $37,900 \text{ mL-H}_2 \text{ min}^{-1} \text{ g-catalyst}^{-1}$. Recently, a series of colloidal metal catalysts were synthesized and used for catalyzing the hydrolysis of KBH_4 [17–20]. For instance, Wang et al. [19] successfully synthesized colloidal Co single-atom catalysts for the effective production of hydrogen from KBH_4 hydrolysis by using ISOBAM (isobutylene-alt maleic anhydride) as a protectant. The synthesized colloidal metal catalysts possess a clearly intrinsic catalytic activity of metal without the influence of support. Besides, those colloidal metal catalysts are stabilized by protective agents and present excellent catalytic activity and recyclability.

It has been widely accepted that the bimetallic catalysts exhibited a high catalytic activity for hydrogen production owing to the synergistic effects between different constituents [21–25]. In detail, the addition of another metal component could modify the electronic structure and then improve the catalytic activity [25,26]. For example, a previous report displayed that the Rh₁₀Ni₉₀ bimetallic nanoparticles (BNPs) possessed a higher catalytic activity for the KBH₄ hydrolysis than that of Rh or Ni MNPs [27]. The catalytic activity of the reported Au/Ni BNPs was several times higher than their corresponding monometallic counterparts [28]. In addition, some non-noble metal catalysts (including Fe [29–31], Ni [18,32,33], Co [19,34], and Cu [35,36]) attract increasing attention owing to their considerable natural abundance, low cost, and competitive catalytic activity. However, the preparation of bimetallic catalysts with noble-free metal constituents is scarcely retrieved.

Herein, we reported a co-reduction method to prepare the ISOBAM-104 stabilized Co/Fe colloidal catalysts, which were then used for the hydrogen production from KBH₄ hydrolysis. The effects of the molar ratio of ISOBAM-104 to metal ion, concentration of metal ion, and molar ratio of Co/Fe were investigated. The as-synthesized ISOBAM-104 stabilized Co₁₀Fe₉₀ colloidal catalysts possess an unexpected catalytic activity for hydrogen production from KBH₄ hydrolysis at room temperature. The activation energy of the as-prepared Co₁₀Fe₉₀ colloidal catalysts towards KBH₄ hydrolysis was calculated by the Arrhenius formula. In addition, the electronic property of metal atoms was investigated based on the DFT calculations.

2. Experimental Section

2.1. Materials

Potassium borohydride (KBH₄), sodium hydroxide (NaOH), iron nitrate nonahydrate (Fe(NO₃)₃·9H₂O) and cobalt nitrate hexahydrate (Co(NO₃)₂·6H₂O) were purchased from Sinopharm Chemical Reagent Co., Ltd., Shanghai, China. ISOBAM-104 (NO. 52032-17-4, Figure S1) was purchased from Kuraray Co., Ltd., Tokyo, Japan. The deionized water was produced via a PINGGUAN ultrapure water purification system (Wuhan, China).

2.2. Preparation of Co/Fe Colloidal Catalysts and Hydrogen Generation

Firstly, certain concentrations of Co(NO₃)₂·6H₂O and Fe(NO₃)₃·9H₂O solution were mixed together in a three-neck flask (Figure S2). Next, a certain amount of ISOBAM-104 was added into the flask and it was then filled with deionized water to 50 mL. After that, the mixed solution was continuously stirred for 24 h at room temperature. Subsequently, the configured KBH₄ and NaOH solution were rapidly added into the above solution to obtain ISOBAM-104 protected Co/Fe BNPs.

The influence of the molar ratio of ISOBAM-104 to metal ion concentration (denoted as R_{ISO} , from 10 to 80), metal ion concentration (from 0.6 to 1.5 mM), and chemical composition (Fe, Co₁₀Fe₉₀, Co₃₀Fe₇₀, Co₅₀Fe₅₀, Co₇₀Fe₃₀, Co₉₀Fe₁₀, and Co) were investigated. The detailed batch compositions are shown in the Table S1. The volume of generated H₂ was measured by an electronic balance, which was automatically recorded based on the displacement level of water every two seconds. During this process, the generated gas was passed through a trap containing concentrated H₂SO₄ to remove H₂O and any NH₃ that might have been generated. The rate of hydrogen generation (k , mL-H₂·min⁻¹) could be obtained from the slope of H₂ volume–time curve in the initial stage of the reaction.

The catalytic activity (mL-H₂·min⁻¹·g-cat⁻¹) could be calculated by the ratio of the hydrogen generation rate (k) to the mass of catalyst (m). It should be noted that the ISOBAM-104 used in this work contains the NH₄⁺ group, which also possesses a catalytic effect for KBH₄ hydrolysis [19,37]. Therefore, under the same condition, the catalytic activities of ISOBAM-104 stabilized Co/Fe colloidal catalysts and ISOBAM-104 (NH₄⁺ group) were measured. The intrinsic catalytic activity value of Co/Fe colloidal catalysts were obtained by subtracting the value of ISOBAM-104 from that of ISOBAM-104 stabilized catalysts. All the catalytic experiments were repeated no less than three times under the identical condition. The average values, which were normalized to mL-H₂ min⁻¹ g-Co⁻¹, were

used to determine the catalytic activity (detailed calculation procedures are provided in the supporting information).

2.3. Material Characterization

UV-vis absorption spectra were recorded at 200–800 nm by a Shimadzu UV-2550 spectrophotometer (Shimadzu Company, Kobe, Japan). Transmission electron microscopy (TEM) and high-resolution transmission electron microscopy (HRTEM) images were collected by using a JEM-2100F (JEOL Company, Tokyo, Japan). The average size of the nanoparticles in each sample was estimated by measuring at least 200 particles from different parts of the grid. Fourier transform infrared (FTIR) spectra were obtained on a FTIR spectrometer (VERTEX 70, Bruker Corporation, Karlsruhe, Germany), and the samples were embedded in KBr pellet. X-ray photoelectron spectroscopy (XPS) measurements were performed on a VG MultiLab 2000 instrument (Thermo Electron Corporation, Massachusetts, USA) equipped with a 300 W Al K α excitation source. The obtained XPS spectra were calibrated using a reference energy of 284.6 eV for the C 1s level and analyzed by Advantage software.

2.4. Density Functional Theory (DFT) Calculation

The spin-polarized density functional theory (DFT) calculations were carried out using a generalized gradient approximation (GGA) with Perdew–Burke–Ernzerhof (PBE) exchange–correlation functional [38], as implemented in the DMol³ package (BIOVIA Company, San Diego, CA, USA) [39]. The double numerical basis set and polarization functions (DNP) were carried out to describe the valence electrons, and an electron relativistic core treatment was used to perform full optimization of the investigated cluster model of Co₆Fe₄₉ BNP without symmetry constraint. The convergence criteria were set to medium quality with a tolerance for the self-consistent field (SCF), optimization energy, maximum force, and maximum displacement of 10^{−5} Ha, 2 × 10^{−5} Ha, 0.004 Ha/Å and 0.005 Å, respectively. The charge analysis was performed on the basis of the Mulliken population distribution scheme [40,41].

3. Results and Discussion

3.1. Effect of R_{ISO} on the Activity of Co/Fe Colloidal Catalysts

To explore the optimized reaction condition, the effect of R_{ISO} on the preparation and catalytic activity of the Co/Fe BNPs was systematically investigated. The TEM images (Figure 1) and size distribution histograms (Figure S3) indicate that the average particle sizes of Co₅₀Fe₅₀ BNPs are about 4.6 nm ($R_{ISO} = 10$), 3.7 nm ($R_{ISO} = 30$), 3.2 nm ($R_{ISO} = 50$), and 2.3 nm ($R_{ISO} = 80$), respectively. Obviously, the average particle size decreases with the increase of R_{ISO} value, which may be ascribed to the fact that the increase of the protective agents could provide a large number of $-\text{COO}^-$ and $-\text{NH}_2$ groups to prevent the agglomeration of particles. Figure 2 displays the catalytic activities of the obtained Co₅₀Fe₅₀ colloidal catalysts for hydrogen production at different R_{ISO} . It can be clearly observed that the Co₅₀Fe₅₀ colloidal catalysts with $R_{ISO} = 50$ possess a higher catalytic value (17,500 mL-H₂ min^{−1} g-Co^{−1}) than those synthesized at $R_{ISO} = 10, 30$, and 80 (6800, 6600, and 5500 mL-H₂ min^{−1} g-Co^{−1}, respectively). This result may be attributed to the fact that Co₅₀Fe₅₀ nanoparticles cannot receive effective protection at low R_{ISO} and are prone to agglomeration, leading to a low catalytic activity. Comparatively, when R_{ISO} was superfluous, the surface of the nanoparticles would be covered by ISOBAM-104, resulting in the decrease of active sites and catalytic activity [28]. Thus, based on the above results, the Co₅₀Fe₅₀ catalysts with moderate particle size and high catalytic activity could be synthesized when $R_{ISO} = 50$.

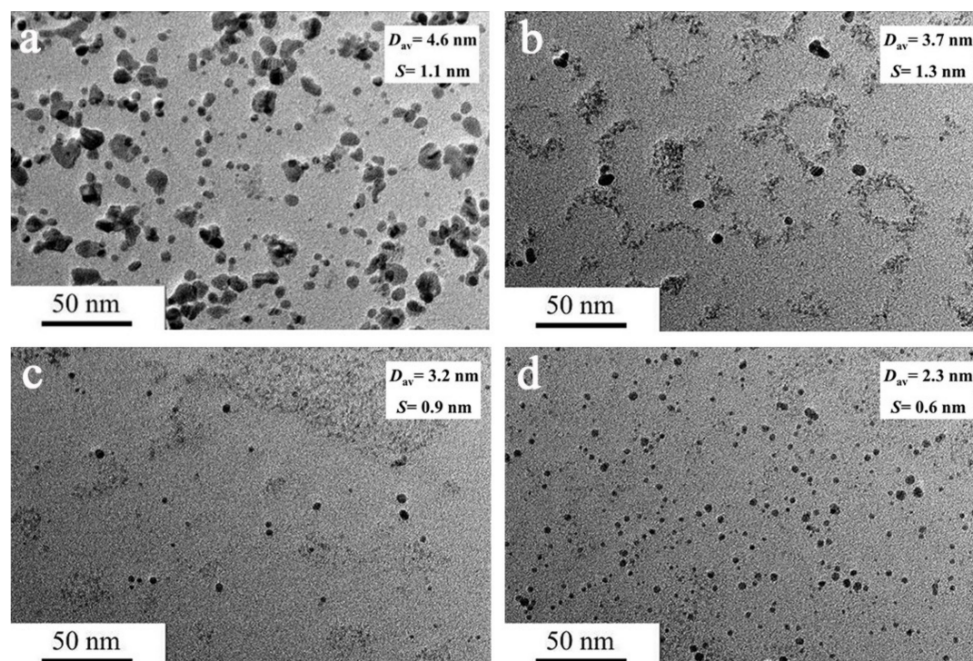


Figure 1. TEM images of $\text{Co}_{50}\text{Fe}_{50}$ colloidal catalysts with various R_{ISO} ($[\text{Co}^{2+} + \text{Fe}^{3+}] = 0.9 \text{ mM}$; $R_{ISO} = 10$ (a), 30 (b), 50 (c), and 80 (d)). (D_{av} : average particle size; S : standard deviation).

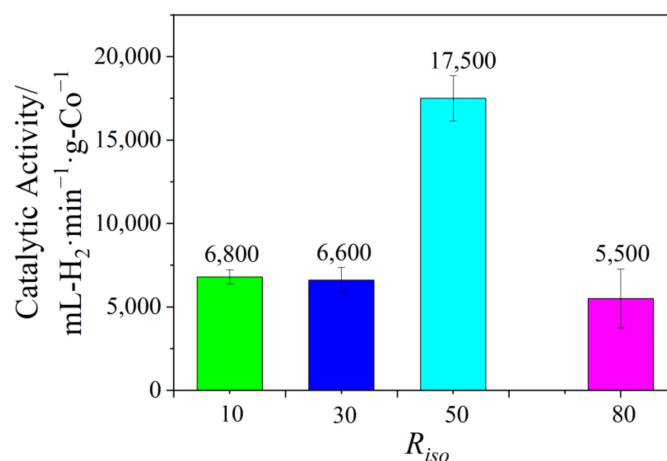


Figure 2. Comparison of catalytic activity of $\text{Co}_{50}\text{Fe}_{50}$ colloidal catalysts with varied R_{ISO} ($[\text{Co}^{2+} + \text{Fe}^{3+}] = 0.9 \text{ mM}$).

3.2. Effect of Metal Ion Concentration on the Activity of Co/Fe Colloidal Catalysts

The effect of ion concentration on the preparation and catalytic activity of $\text{Co}_{50}\text{Fe}_{50}$ colloidal catalysts was also investigated. TEM morphologies and size distribution histograms of the as-prepared $\text{Co}_{50}\text{Fe}_{50}$ BNPs are presented in Figure 3 and Figure S4. The average particle sizes are about 2.3, 3.2, 2.6, and 3.4 nm at the metal ion concentrations of 0.6, 0.9, 1.2, and 1.5 mM, respectively. It is found that the metal ion concentration exerts a significant influence on the particle size of the obtained catalysts. Although the $\text{Co}_{50}\text{Fe}_{50}$ BNPs with the smaller particle sizes are obtained at the metal ion concentrations of 0.6 mM, the low concentration of metal ion impedes the large-scale preparation of catalysts. Hence, the concentration of metal ion is set as 1.2 mM in the following discussion.

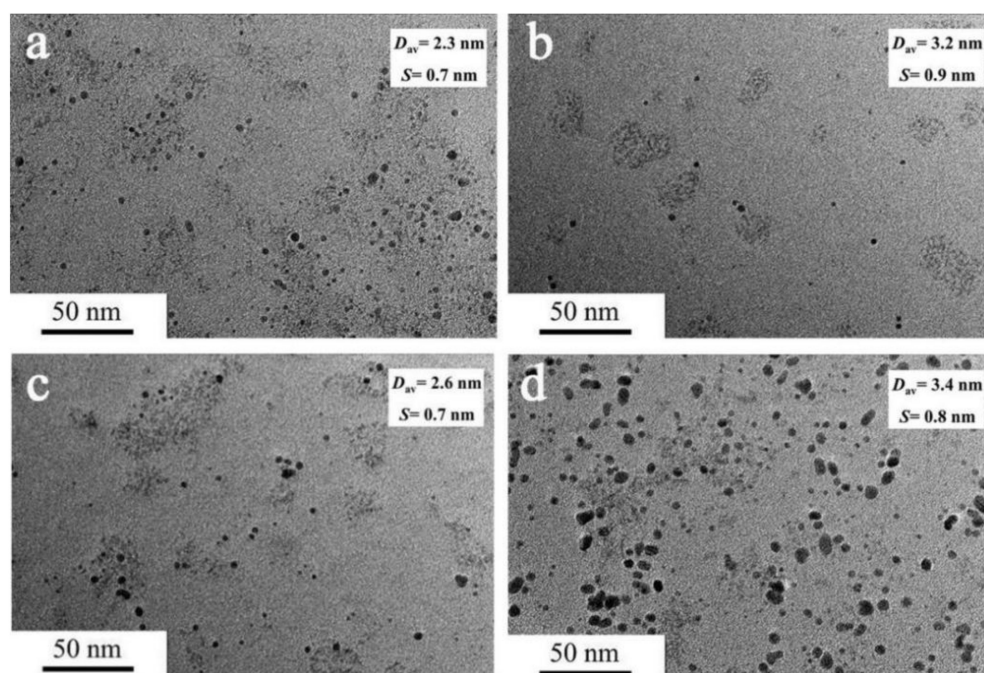


Figure 3. TEM images and size distribution histograms of $\text{Co}_{50}\text{Fe}_{50}$ colloidal catalysts synthesized with different ion concentrations ($[\text{Co}^{2+} + \text{Fe}^{3+}] = 0.6$ (a), 0.9 (b), 1.2 (c), and 1.5 (d) mM). (D_{av} : average particle size; S: standard deviation).

3.3. Effect of Chemical Composition on the Activity of Co/Fe Colloidal Catalysts

The UV-vis spectra of the obtained Co/Fe BNPs with various compositions are shown in Figure S5. It was found that no surface plasma resonance peak of Fe or Co nanoparticles could be detected, which agrees with the previous reports [26,27,42]. The spectra of the dispersed Co/Fe nanoparticles BNPs with a featureless absorbance were located between the spectra of single Co and Fe nanoparticles, exhibiting a featureless absorbance. These obvious differences of the absorbance at various Fe content suggest the formation of alloy-structured Co/Fe BNPs. Figure 4 presents the TEM images of the obtained Co/Fe BNPs at various Co/Fe atomic ratios. It can be clearly seen that the particles possessed a sphere-like morphology. The average sizes of ISOBAM-104 stabilized Fe, $\text{Co}_{10}\text{Fe}_{90}$, $\text{Co}_{30}\text{Fe}_{70}$, $\text{Co}_{50}\text{Fe}_{50}$, $\text{Co}_{70}\text{Fe}_{30}$, $\text{Co}_{90}\text{Fe}_{10}$, and Co colloidal catalysts are respectively about 3.0, 3.2, 2.6, 2.6, 2.2, 2.5, and 1.8 nm (Figure S6). The corresponding catalytic activities of the above colloidal catalysts are displayed in Figure 5. By comparison, the above-mentioned Co/Fe BNPs presented a superior catalytic activity than that of Co or Fe MNPs. More importantly, the catalytic activity of the $\text{Co}_{10}\text{Fe}_{90}$ colloidal catalysts reaches up to $37,900 \text{ mL-H}_2 \text{ min}^{-1} \text{ g-Co}^{-1}$, which is about 5 and 4 times higher than that of Fe ($7400 \text{ mL-H}_2 \text{ min}^{-1} \text{ g-Fe}^{-1}$) and Co ($9600 \text{ mL-H}_2 \text{ min}^{-1} \text{ g-Co}^{-1}$), respectively. Based on the above results, the desirable Co/Fe colloidal catalysts with high catalytic performance can be synthesized at the chemical composition of $\text{Co}_{10}\text{Fe}_{90}$, $R_{ISO} = 50$, and ion concentrations of 1.2 mM.

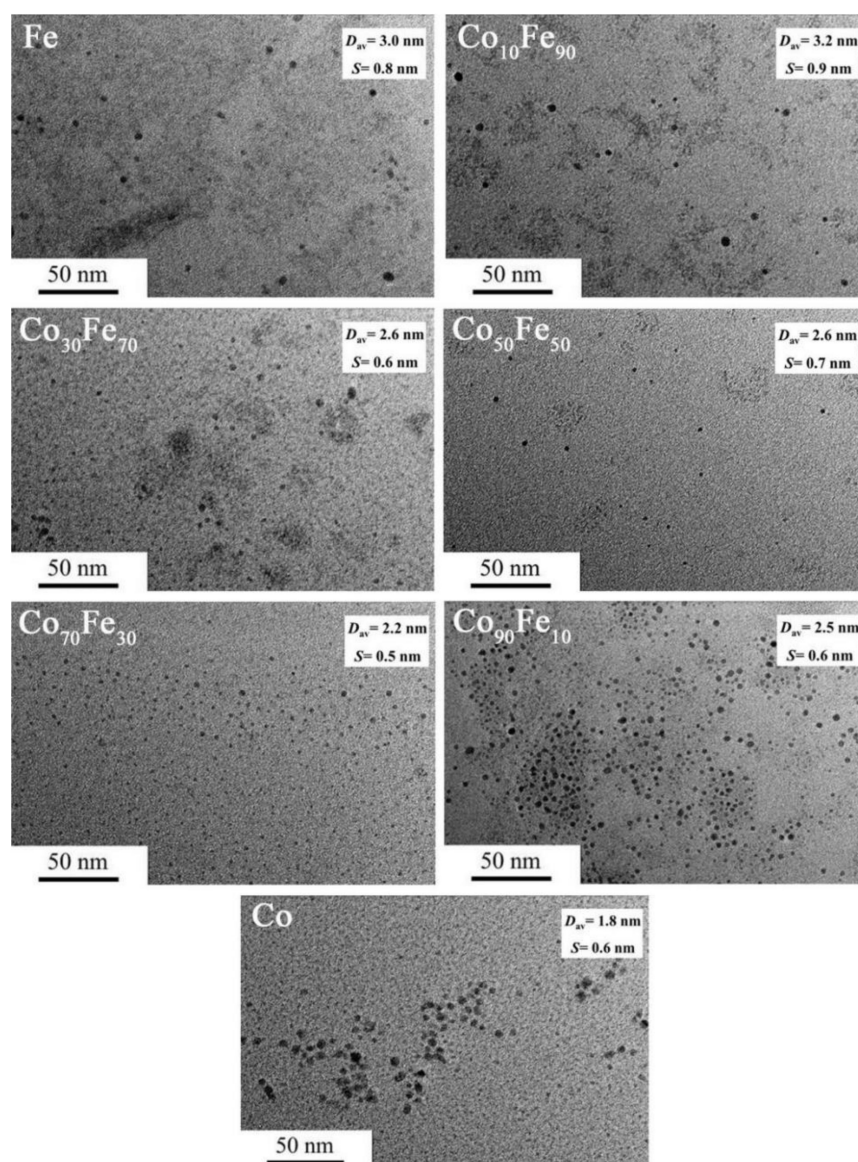


Figure 4. TEM images of Co/Fe colloidal catalysts synthesized with various chemical compositions ($R_{ISO} = 50$, $[Co^{2+} + Fe^{3+}] = 1.2$ mM). (D_{av} : average particle size; S : standard deviation).

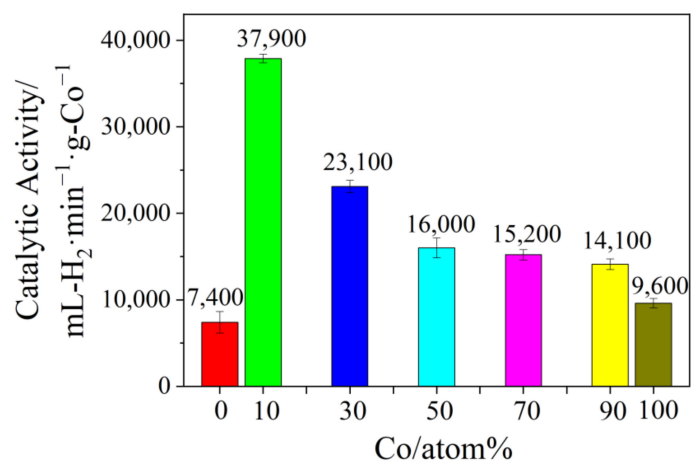


Figure 5. Comparison of catalytic activity of Co/Fe colloidal catalysts with various chemical compositions ($R_{ISO} = 50$, $[Co^{2+} + Fe^{3+}] = 1.2$ mM).

The structure of the obtained $\text{Co}_{10}\text{Fe}_{90}$ colloidal catalysts was further characterized by the high-resolution transmission electron microscope (HRTEM). As shown in Figure 6, the interplanar spacings of the four individual randomly-chosen Co/Fe BNPs are measured as 0.168, 0.172, 0.174, and 0.169 nm, respectively. These values are inconsistent with the theoretical interplanar spacing values of Co and Fe (Table S2). However, it is worth noting that this measured interplanar spacing located between the interplanar distance of Co (200) and Fe (200) (Table S3), suggests the alloy structure of the formed Co/Fe BNPs.

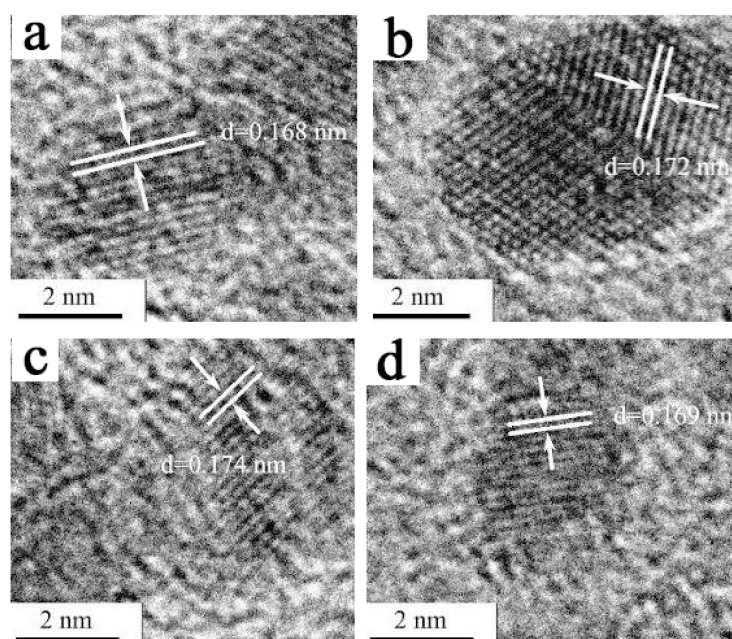


Figure 6. HRTEM images (a–d) of $\text{Co}_{10}\text{Fe}_{90}$ colloidal catalysts ($R_{\text{ISO}} = 50$, $[\text{Co}^{2+} + \text{Fe}^{3+}] = 1.2 \text{ mM}$). (HRTEM images of a–d correspond to four individual randomly-chosen Co/Fe bimetallic nanoparticles.)

In order to understand the protecting role of ISOBAM-104 in the catalysts stabilization, the FTIR spectra of ISOBAM-104 stabilized Co/Fe catalysts, ISOBAM-104, $\text{Co}(\text{NO}_3)_2$, and $\text{Fe}(\text{NO}_3)_3$ are displayed in Figure S7. The absorption peak at 1400, 1680, 2300, and 3400 cm^{-1} , respectively, correspond to the stretching vibration of $-\text{OH}$, $-\text{COOH}$, $-\text{CO}_2$, and the $-\text{NH}_2$ group of ISOBAM-104. By comparison, it can be clearly seen that the $-\text{COOH}$ group of ISOBAM-104 disappeared, while the $-\text{OH}$ and $-\text{NH}_2$ group still appeared in the ISOBAM-104 stabilized Co/Fe catalysts, demonstrating that the $-\text{NH}_2$ group in ISOBAM-104 should play a protective role on the as-prepared metal catalyst [18].

3.4. Kinetic Study and Catalytic Mechanism of Co/Fe Colloidal Catalysts

To calculate the apparent activation energy (E_a), the catalytic performance of $\text{Co}_{10}\text{Fe}_{90}$ colloidal catalysts were evaluated under the perturbation of the reaction temperature. As shown in Figure S8, it can be seen that the catalytic activity of the $\text{Co}_{10}\text{Fe}_{90}$ colloidal catalysts increases from 8400 to 15,200 $\text{mL-H}_2 \text{ min}^{-1} \text{ g-catalyst}^{-1}$ as the temperature increases from 293 to 308 K. The E_a is calculated by using the Arrhenius method [43]. As shown in Figure 7, the slope of the linear curve between the natural logarithm of catalytic activity and the reciprocal of temperature is $-E_a/R$, where R is the universal gas constant. The calculated E_a of $\text{Co}_{10}\text{Fe}_{90}$ colloidal catalysts is $14.6 \pm 0.7 \text{ kJ mol}^{-1}$, which is much lower than most of the reported metal-based catalysts (Table 1). Interestingly, the corresponding catalytic activity of the $\text{Co}_{10}\text{Fe}_{90}$ colloidal catalysts is much higher than these metal-based catalysts. Thus, it can be confirmed that the excellent catalytic activity of $\text{Co}_{10}\text{Fe}_{90}$ colloidal catalysts is closely related to the lower activation energy towards KBH_4 hydrolysis.

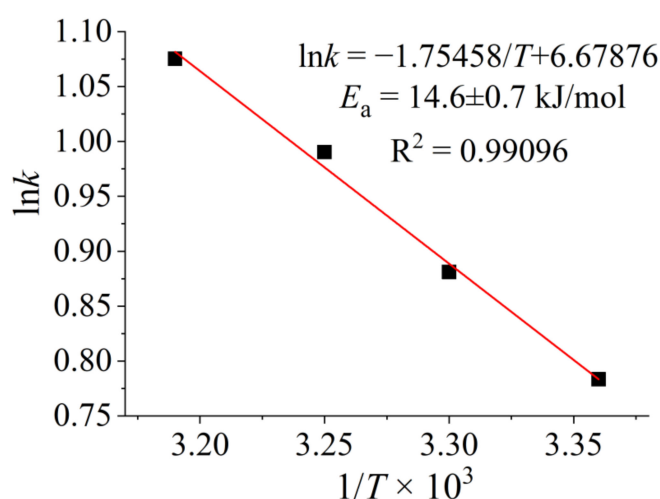


Figure 7. The apparent activation energy (E_a) of $\text{Co}_{10}\text{Fe}_{90}$ colloidal catalysts for KBH_4 hydrolysis at 293–308 K.

Table 1. Comparison of the apparent activation energy between the $\text{Co}_{10}\text{Fe}_{90}$ colloidal catalysts and other catalysts in the previously reported literature.

Catalyst	Reactant	Activation Energy (kJ mol^{-1})	Catalytic Activity ($\text{mL-H}_2 \text{ min}^{-1} \text{ g-cat.}^{-1}$)	Reference
Co/Fe	KBH_4	14.6	37,900	Present work
Ni	KBH_4	41.3	12,400	[18]
Rh/Ni	KBH_4	47.2	11,580	[27]
Co-O-P	NaBH_4	63	4850	[44]
Ag/Ni	NaBH_4	16.2	2333	[45]
Co-Ni-P	NaBH_4	31.2	6681	[46]
Co-B	NaBH_4	37.57	2649	[47]
Co-B	NaBH_4	30	5310	[48]
CoO-Co ₂ P	NaBH_4	27.4	3940	[49]

An XPS measurement was subsequently carried out to clarify the elemental composition and valence state of the $\text{Co}_{10}\text{Fe}_{90}$ BNPs. In Figure S9a, the element of Co, Fe, O, N, C, and B are detected in the obtained Co/Fe colloidal catalysts. The high-resolution XPS spectra of Co 2p (Figure S9b) shows that the electron binding energy of $\text{Co}^0 2p_{3/2}$ (776.0 eV) is about 2.3 eV lower than that of the bulk Co (778.3 eV), indicating a negatively-charged characteristic of Co atoms in $\text{Co}_{10}\text{Fe}_{90}$ BNPs. Meanwhile, the electron binding energy of $\text{Fe}^0 2p_{3/2}$ (708.5 eV) was about 1.8 eV higher than that of the bulk Fe (706.7 eV), suggesting that the Fe atoms were positively charged (Figure S9c). The negative shift of the $\text{Co}^0 2p_{3/2}$ binding energy and positive shift of the $\text{Fe}^0 2p_{3/2}$ binding energy might be ascribed to the electron charge transfer occurring between Fe and Co atoms [23,24,26,50,51]. To further confirm the electron transfer effect, DFT calculations were employed to investigate the electronic states of each atom in the $\text{Co}_6\text{Fe}_{49}$ alloy nanoparticles [52]. As shown in Figure 8a, the Co atoms are negatively charged (−0.091 eV), while the Fe atoms are positively charged (0.029 or 0.021 eV), which is matched well with the above XPS result. Based on above discussions and the related literature [23,27], a plausible mechanism for the high catalytic performance of Co/Fe colloidal catalysts could be proposed. Due to the charge transfer between Fe atoms and Co atoms (Figure 8b), the negatively charged Co atoms are conducive to the fracture of H–O bonds in H_2O molecules, and the positively charged Fe atoms could promote the B–H bond breaking in KBH_4 molecules. As a result, the catalytic activity of Co/Fe colloidal catalysts for KBH_4 hydrolysis could be markedly enhanced under the synergistic effect of Fe and Co atoms.

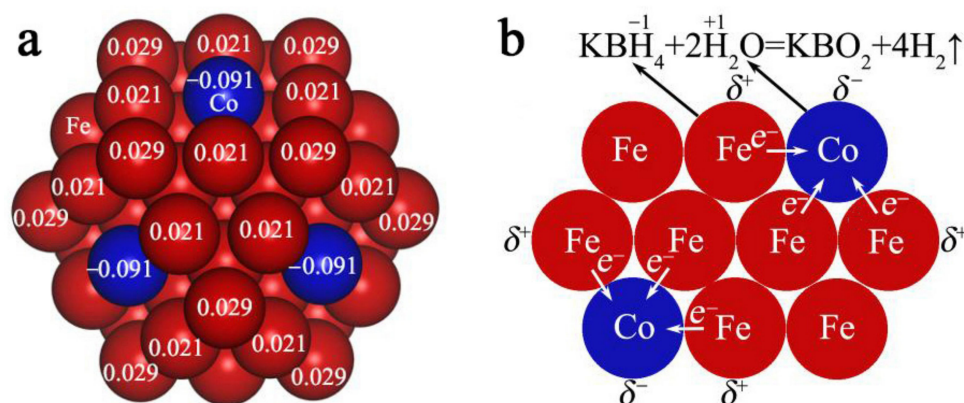


Figure 8. Catalytic mechanism. (a) DFT calculations of the electronic structure of $\text{Co}_6\text{Fe}_{49}$ nanoparticles (red, Fe; and blue, Co). (b) Schematic illustration of the possible electron charge transfer effects between Co and Fe atoms in the $\text{Co}_6\text{Fe}_{49}$ nanoparticles.

4. Conclusions

In summary, the ISOBAM-104 stabilized Co/Fe colloidal catalysts are successfully synthesized for hydrogen generation by a simple co-reduction method via using ISOBAM-104 as a protective agent, and $\text{Co}(\text{NO}_3)_2 \cdot 6\text{H}_2\text{O}$, $\text{Fe}(\text{NO}_3)_3 \cdot 9\text{H}_2\text{O}$, and KBH_4 as starting materials. The catalytic activities of the obtained Co/Fe colloidal catalysts could reach up to $37,900 \text{ mL-H}_2 \text{ min}^{-1} \text{ g-Co}^{-1}$ at the chemical composition of $\text{Co}_{10}\text{Fe}_{90}$, $R_{\text{ISO}} = 50$, and ion concentrations of 1.2 mM, which is superior to their corresponding monometallic nanoparticles. The excellent catalytic activity of $\text{Co}_{10}\text{Fe}_{90}$ colloidal catalysts is mainly attributed to their lower activation energy towards KBH_4 hydrolysis, and the charge transfer effect between Fe and Co atoms. This finding could provide a deeper insight for developing the economic, highly active, and recyclable bimetallic catalysts.

Supplementary Materials: The following supporting information can be downloaded at: <https://www.mdpi.com/article/10.3390/nano12172998/s1>, Figure S1: The chemical structure of ISOBAM-104; Figure S2: The schematic diagram of experimental device for KBH_4 hydrolysis reaction; Figure S3: Particles size distribution histograms of $\text{Co}_{50}\text{Fe}_{50}$ colloidal catalysts with various R_{ISO} ($[\text{Co}^{2+} + \text{Fe}^{3+}] = 0.9 \text{ mM}$; $R_{\text{ISO}} = 10$ (a), 30 (b), 50 (c), and 80 (d)); Figure S4: Particles size distribution histograms of $\text{Co}_{50}\text{Fe}_{50}$ colloidal catalysts synthesized with various ion concentrations ($R_{\text{ISO}} = 50$; $[\text{Co}^{2+} + \text{Fe}^{3+}] = 0.6$ (a), 0.9 (b), 1.2 (c), and 1.5 (d) mM); Figure S5: UV-vis spectra of Co/Fe BNPs, Co and Fe nanoparticles; Figure S6: Particles size distribution histograms of Co/Fe colloidal catalysts synthesized with various chemical compositions ($R_{\text{ISO}} = 50$, $[\text{Co}^{2+} + \text{Fe}^{3+}] = 1.2 \text{ mM}$); Figure S7: FTIR spectra of ISOBAM-104, $\text{Co}(\text{NO}_3)_2$, $\text{Fe}(\text{NO}_3)_3$, and $\text{Co}_{10}\text{Fe}_{90}$ colloidal catalysts; Figure S8: Effect of temperature on the catalytic performance of $\text{Co}_{10}\text{Fe}_{90}$ colloidal catalysts; Figure S9: XPS spectra of $\text{Co}_{30}/\text{Fe}_{70}$ colloidal catalysts: (a) total spectra, (b) Co 2p, and (c) Fe 2p; Table S1: Batch compositions and processing conditions for the preparation of ISOBAM-104 stabilized Co/Fe colloidal catalysts; Table S2: Lattice spacing and indexed reflection planes of Co and Fe; Table S3: Lattice spacing and indexed reflection planes of Co/Fe colloidal catalysts determined by HRTEM.

Author Contributions: K.G.: investigation, formal analysis, and writing—original draft preparation; Q.Z.: investigation and writing—original draft preparation; Z.H. (Zhong Huang): supervision, writing—review and editing; Z.H. (Zhenxia Huang): methodology and investigation. H.Z.: methodology, writing—review and editing, project administration and funding acquisition; J.W.: investigation and software. Q.J.: project administration; S.Z.: project administration and funding acquisition. All authors have read and agreed to the published version of the manuscript.

Funding: This research was funded by National Natural Science Foundation of China (Grant No. 52072274, 51872210, and 52102017), Program of Hubei Province, China (Contract No. 2017CFA004 and T201602).

Institutional Review Board Statement: Not applicable.

Informed Consent Statement: Not applicable.

Acknowledgments: This work was financially supported by National Natural Science Foundation of China, Program of Hubei Province, China.

Conflicts of Interest: The authors declare no conflict of interest.

References

1. Fu, F.Y.; Wang, C.L.; Wang, Q.; Martinez-Villacorta, A.M.; Escobar, A.; Chong, H.B.; Wang, X.; Moya, S.; Salmon, L.; Fouquet, E.; et al. Highly selective and sharp volcano-type synergistic Ni₂Pt@ZIF-8-catalyzed hydrogen evolution from ammonia borane hydrolysis. *J. Am. Chem. Soc.* **2018**, *140*, 10034–10042. [[CrossRef](#)]
2. Kılınça, D.; Şahinb, Ö. Metal-Schiff Base complex catalyst in KBH₄ hydrolysis reaction for hydrogen production. *Int. J. Hydrogen Energ.* **2019**, *44*, 18848–18857. [[CrossRef](#)]
3. Kang, J.X.; Chen, T.W.; Zhang, D.F.; Guo, L. PtNiAu trimetallic nanoalloys enabled by a digestive-assisted process as highly efficient catalyst for hydrogen generation. *Nano Energy* **2016**, *23*, 145–152. [[CrossRef](#)]
4. Balčiūnaitė, A.; Sukackienė, Z.; Antanavičiūtė, K.; Vaičiūnienė, J.; Naujokaitis, A.; Tamašauskaitė, L.; Norkus, E. Investigation of hydrogen generation from sodium borohydride using different cobalt catalysts. *Int. J. Hydrogen Energ.* **2021**, *46*, 1989–1996. [[CrossRef](#)]
5. Wang, T.H.; Jiang, T.T.; Zhang, H.F.; Zhao, Y. Advances in catalysts for hydrogen production by methanolysis of sodium borohydride. *Int. J. Hydrogen Energ.* **2022**, *47*, 14589–14610. [[CrossRef](#)]
6. Luo, L.M.; Yang, M.; Chen, G.W. Continuous synthesis of TiO₂-supported noble metal nanoparticles and their application in ammonia borane hydrolysis. *Chem. Eng. Sci.* **2022**, *251*, 117479. [[CrossRef](#)]
7. Zhang, X.M.; Zhang, Q.M.; Peng, Y.M.; Ma, X.Y.; Fan, G.Y. Oxygen vacancies and morphology engineered Co₃O₄ anchored Ru nanoparticles as efficient catalysts for ammonia borane hydrolysis. *Int. J. Hydrogen Energ.* **2022**, *47*, 7793–7801. [[CrossRef](#)]
8. Wang, J.; Chen, Y.M.; Guan, S.Y.; Shi, J.C.; Li, M.B.; Liu, B.Z. Tuning Fe doping Co/CoO_x amorphous nanofilms to enhance the hydrolytic activity towards ammonia borane. *J. Alloy. Compd.* **2022**, *913*, 165215. [[CrossRef](#)]
9. Yadav, M.; Xu, Q. Liquid-phase chemical hydrogen storage materials. *Energy Environ. Sci.* **2012**, *5*, 9698–9725. [[CrossRef](#)]
10. Lang, C.G.; Jia, Y.; Yao, X.D. Recent advances in liquid-phase chemical hydrogen storage. *Energy Storage Mater.* **2020**, *26*, 290–312. [[CrossRef](#)]
11. Sun, Q.M.; Wang, N.; Xu, Q.; Yu, J.H. Nanopore-supported metal nanocatalysts for efficient hydrogen generation from liquid-phase chemical hydrogen storage materials. *Adv. Mater.* **2020**, *32*, 2001818. [[CrossRef](#)]
12. Kilinc, D.; Sahin, O. High volume hydrogen evolution from KBH₄ hydrolysis with palladium complex catalyst. *Renew. Energ.* **2020**, *161*, 257–264. [[CrossRef](#)]
13. Moussa, G.; Moury, R.; Demirci, U.B.; Şener, T.; Miele, P. Boron-based hydrides for chemical hydrogen storage. *Int. J. Energ. Res.* **2013**, *37*, 825–842. [[CrossRef](#)]
14. Orimo, S.; Nakamori, Y.; Eliseo, J.R.; Züttel, A.; Jensen, C.M. Complex hydrides for hydrogen storage. *Chem. Rev.* **2007**, *107*, 4111–4132. [[CrossRef](#)]
15. Zhao, Y.; Wang, T.H.; Wang, Y.B.; Hao, R.L.; Hui, W.T. Simultaneous absorption and hydrogenation of CO₂ from flue gas by KBH₄ catalyzed by nickel nanoparticles supported on TiO₂. *Chem. Eng. J.* **2020**, *380*, 122523. [[CrossRef](#)]
16. Fujioka, D.; Ikedab, S.; Akamatsuc, K.; Nawafunec, H.; Kojima, K. Preparation of Ni nanoparticles by liquid-phase reduction to fabricate metal nanoparticle–polyimide composite films. *RSC Adv.* **2019**, *9*, 6438–6443. [[CrossRef](#)]
17. Guan, K.K.; Wang, L.Q.; Huang, L.; Lei, W.; Jia, Q.L.; Zhang, H.J.; Zhang, S.W. Synthesis and high catalytic activity of ISOBAM-104 stabilized Fe colloidal catalysts for hydrogen generation. *Catal. Today* **2021**, *374*, 20–28. [[CrossRef](#)]
18. Pei, Y.T.; Wang, L.Q.; Huang, L.; Hu, Y.T.; Jia, Q.L.; Zhang, H.J.; Zhang, S.W. ISOBAM-stabilized Ni²⁺ colloidal catalysts: High catalytic activities for hydrogen generation from hydrolysis of KBH₄. *Nanotechnology* **2020**, *31*, 134003. [[CrossRef](#)]
19. Wang, J.K.; Huang, Z.X.; Lu, L.L.; Jia, Q.L.; Huang, L.; Chang, S.; Zhang, M.Y.; Zhang, Z.T.; Li, S.; He, D.S.; et al. Colloidal Co single-atom catalyst: A facile synthesis strategy and high catalytic activity for hydrogen generation. *Green Chem.* **2020**, *22*, 1269–1274. [[CrossRef](#)]
20. Qu, Y.T.; Li, Z.J.; Chen, W.X.; Lin, Y.; Yuan, T.W.; Yang, Z.K.; Zhao, C.M.; Wang, J.; Zhao, C.; Wang, X.; et al. Direct transformation of bulk copper into copper single sites via emitting and trapping of atoms. *Nat. Catal.* **2018**, *1*, 781–786. [[CrossRef](#)]
21. Zhang, J.K.; Chen, W.Y.; Ge, H.B.; Chen, C.Q.; Yan, W.J.; Gao, Z.; Gan, J.; Zhang, B.Y.; Duan, X.Z.; Qin, Y. Synergistic effects in atomic-layer-deposited PtCox/CNTs catalysts enhancing hydrolytic dehydrogenation of ammonia borane. *Appl. Catal. B Environ.* **2018**, *235*, 256–263. [[CrossRef](#)]
22. Li, J.; Zhu, Q.L.; Xu, Q. Non-noble bimetallic CuCo nanoparticles encapsulated in the pores of metal–organic frameworks: Synergetic catalysis in the hydrolysis of ammonia borane for hydrogen generation. *Catal. Sci. Technol.* **2015**, *5*, 525–530. [[CrossRef](#)]
23. Huang, L.; Jiao, C.P.; Wang, L.Q.; Huang, Z.L.; Liang, F.; Liu, S.M.; Wang, Y.H.; Zhang, H.J.; Zhang, S.W. Preparation of Rh/Ag bimetallic nanoparticles as effective catalyst for hydrogen generation from hydrolysis of KBH₄. *Nanotechnology* **2018**, *29*, 044002. [[CrossRef](#)] [[PubMed](#)]

24. Wang, X.F.; Huang, Z.L.; Lu, L.L.; Zhang, H.J.; Cao, Y.N.; Gu, Y.J.; Cheng, Z.; Zhang, S.W. Preparation and catalytic activities of Au/Co bimetallic nanoparticles for hydrogen generation from NaBH₄ solution. *J. Nanosci. Nanotech.* **2015**, *15*, 2770–2776. [[CrossRef](#)]
25. Singh, A.K.; Xu, Q. Synergistic catalysis over bimetallic alloy nanoparticles. *Chemcatchem* **2013**, *5*, 652–676. [[CrossRef](#)]
26. Jiao, C.P.; Huang, Z.L.; Wang, X.F.; Zhang, H.J.; Lu, L.L.; Zhang, S.W. Synthesis of Ni/Au/Co trimetallic nanoparticles and their catalytic activity for hydrogen generation from alkaline sodium borohydride aqueous solution. *RSC Adv.* **2015**, *5*, 34364–34371. [[CrossRef](#)]
27. Wang, L.Q.; Huang, L.; Jiao, C.P.; Huang, Z.L.; Liang, F.; Liu, S.M.; Wang, Y.H.; Zhang, H.J. Preparation of Rh/Ni bimetallic nanoparticles and their catalytic activities for hydrogen generation from hydrolysis of KBH₄. *Catalysts* **2017**, *7*, 125. [[CrossRef](#)]
28. Wang, X.F.; Sun, S.R.; Huang, Z.L.; Zhang, H.J.; Zhang, S.W. Preparation and catalytic activity of PVP-protected Au/Ni bimetallic nanoparticles for hydrogen generation from hydrolysis of basic NaBH₄ solution. *Int. J. Hydrogen Energ.* **2014**, *39*, 905–916. [[CrossRef](#)]
29. Lu, Z.H.; Li, J.P.; Zhu, A.L.; Yao, Q.L.; Huang, W.; Zhou, R.Y.; Zhou, R.F.; Chen, X.S. Catalytic hydrolysis of ammonia borane via magnetically recyclable copper iron nanoparticles for chemical hydrogen storage. *Int. J. Hydrogen Energ.* **2013**, *38*, 5330–5337. [[CrossRef](#)]
30. Yan, J.M.; Zhang, X.B.; Han, S.; Shioyama, H.; Xu, Q. Iron-nanoparticle-catalyzed hydrolytic dehydrogenation of ammonia borane for chemical hydrogen storage. *Angew. Chem. Int. Edit.* **2008**, *47*, 2287–2289. [[CrossRef](#)]
31. Xu, Q.; Chandra, M. Catalytic activities of non-noble metals for hydrogen generation from aqueous ammonia–borane at room temperature. *J. Power Sources* **2006**, *163*, 364–370. [[CrossRef](#)]
32. Yan, J.M.; Zhang, X.B.; Han, S.; Shioyama, H.; Xu, Q. Synthesis of longtime water/air-stable Ni nanoparticles and their high catalytic activity for hydrolysis of ammonia borane for hydrogen generation. *Inorg. Chem.* **2009**, *48*, 7389–7393. [[CrossRef](#)]
33. Umegaki, T.; Yan, J.M.; Zhang, X.B.; Shioyama, H.; Kuriyama, N.; Xu, Q. Hollow Ni–SiO₂ nanosphere-catalyzed hydrolytic dehydrogenation of ammonia borane for chemical hydrogen storage. *J. Power Sources* **2009**, *191*, 209–216. [[CrossRef](#)]
34. Rakap, M.; Özkaz, S. Hydrogen generation from the hydrolysis of ammonia-borane using intrazeolite cobalt(0) nanoclusters catalyst. *Int. J. Hydrogen Energ.* **2010**, *35*, 3341–3346. [[CrossRef](#)]
35. Yao, Q.L.; Lu, Z.H.; Zhang, Z.J.; Chen, X.S.; Lan, Y.Q. One-pot synthesis of core-shell Cu@SiO₂ nanospheres and their catalysis for hydrolytic dehydrogenation of ammonia borane and hydrazine borane. *Sci. Rep.* **2015**, *4*, 7597. [[CrossRef](#)]
36. Kalidindi, S.B.; Sanyala, U.; Jagirdar, B.R. Nanostructured Cu and Cu@Cu₂O core shell catalysts for hydrogen generation from ammonia–borane. *Phys. Chem. Chem. Phys.* **2008**, *40*, 5870–5874. [[CrossRef](#)]
37. Lu, L.L.; Zhang, H.J.; Zhang, S.W.; Li, F.L. A family of high-efficiency hydrogen-generation catalysts based on ammonium species. *Angew. Chem. Int. Edit.* **2015**, *54*, 9328–9332. [[CrossRef](#)]
38. Brajczewska, M.; Vieira, A.; Fiolhais, C.; Perdew, J.P. Volume shift and charge instability of simple-metal clusters. *Prog. Surf. Sci.* **1996**, *53*, 305–313. [[CrossRef](#)]
39. Delley, B. DMol³ DFT studies: From molecules and molecular environments to surfaces and solids. *Comput. Mater. Sci.* **2000**, *17*, 122–126. [[CrossRef](#)]
40. Reed, A.E.; Weinstock, R.B.; Weinhold, F. Natural population analysis. *J. Chem. Phys.* **1985**, *83*, 735–746. [[CrossRef](#)]
41. Clark, A.E.; Sonnenberg, J.L.; Hay, P.J.; Martin, R.L. Density and wave function analysis of actinide complexes: What can fuzzy atom, atoms-in-molecules, Mulliken, Löwdin, and natural population analysis tell us? *J. Chem. Phys.* **2004**, *121*, 2563–2570. [[CrossRef](#)]
42. Zhang, H.J.; Cao, Y.N.; Lu, L.L.; Cheng, Z.; Zhang, S.W. Trimetallic Au/Pt/Rh nanoparticles as highly active catalysts for aerobic glucose oxidation. *Metall. Mater. Trans. B* **2014**, *46*, 523–530. [[CrossRef](#)]
43. Zhang, H.J.; Deng, X.G.; Jiao, C.P.; Lu, L.L.; Zhang, S.W. Preparation and catalytic activities for H₂O₂ decomposition of Rh/Au bimetallic nanoparticles. *Mater. Res. Bull.* **2016**, *79*, 29–35. [[CrossRef](#)]
44. Wei, L.; Dong, X.L.; Yang, Y.M.; Shi, Q.Y.; Lu, Y.H.; Liu, H.Y.; Yu, Y.N.; Zhang, M.H.; Qi, M.; Wang, Q. Co-O-P composite nanocatalysts for hydrogen generation from the hydrolysis of alkaline sodium borohydride solution. *Int. J. Hydrogen Energ.* **2020**, *45*, 10745–10753. [[CrossRef](#)]
45. Al-Thabaiti, S.A.; Khan, Z.; Malik, M.A. Bimetallic Ag-Ni nanoparticles as an effective catalyst for hydrogen generation from hydrolysis of sodium borohydride. *Int. J. Hydrogen Energ.* **2019**, *44*, 16452–16466. [[CrossRef](#)]
46. Li, J.H.; Hong, X.Y.; Wang, Y.L.; Luo, Y.M.; Li, B.; Huang, P.R.; Zou, Y.J.; Chu, H.L.; Zheng, S.Y.; Sun, L.X.; et al. A modified ‘skeleton/skin’ strategy for designing CoNiP nanosheets arrayed on graphene foam for on/off switching of NaBH₄ hydrolysis. *RSC Adv.* **2020**, *10*, 26834–26842. [[CrossRef](#)]
47. Xu, J.A.; Du, X.X.; Wei, Q.L.; Huang, Y.M. Efficient Hydrolysis of sodium borohydride by Co-B supported on nitrogen-doped carbon. *Chemistryselect* **2020**, *5*, 6683–6690. [[CrossRef](#)]
48. Wang, X.P.; Liao, J.J.; Li, H.; Wang, H.; Wang, R.F.; Pollet, B.G.; Ji, S. Highly active porous Co-B nanoalloy synthesized on liquid-gas interface for hydrolysis of sodium borohydride. *Int. J. Hydrogen Energ.* **2018**, *43*, 17543–17555. [[CrossRef](#)]
49. Liu, H.Y.; Shi, Q.Y.; Yang, Y.M.; Yu, Y.N.; Zhang, Y.; Zhang, M.S.; Wei, L.; Lu, Y.H. CoO-Co₂P composite nanosheets as highly active catalysts for sodium borohydride hydrolysis to generate hydrogen. *Funct. Mater. Lett.* **2020**, *13*, 2051025. [[CrossRef](#)]
50. Zhang, H.J.; Wang, L.Q.; Lu, L.L.; Toshima, N. Preparation and catalytic activity for aerobic glucose oxidation of crown jewel structured Pt/Au bimetallic nanoclusters. *Sci. Rep.* **2016**, *6*, 30752. [[CrossRef](#)]

51. Zhang, H.J.; Lu, L.L.; Kawashima, K.; Okumura, M.; Haruta, M.; Toshima, N. Synthesis and catalytic activity of crown jewel-structured (IrPd)/Au trimetallic nanoclusters. *Adv. Mater.* **2014**, *27*, 1383–1388. [[CrossRef](#)] [[PubMed](#)]
52. Zhang, H.J.; Watanabe, T.; Okumura, M.; Haruta, M.; Toshima, N. Catalytically highly active top gold atom on palladium nanocluster. *Nat. Mater.* **2012**, *11*, 49–52. [[CrossRef](#)] [[PubMed](#)]